batteries

MDPI

Article

Two-Dimensional VO_2 Nanosheets with a Controllable Crystalline-Preferred Orientation for High-Performance Zinc-Ion Batteries

Shanshan Shi [1,2,*], Yang Yu [2], Xiaochen Feng [2], Ruijuan Qi [3] and Yufeng Zhao [1,*]

[1] Institute for Sustainable Energy, College of Sciences, Shanghai University, Shanghai 200444, China
[2] Key Laboratory of Applied Chemistry, Yanshan University, Qinhuangdao 066004, China
[3] Key Laboratory of Polar Materials and Devices (MOE), Department of Optoelectronics, East China Normal University, Shanghai 200241, China
* Correspondence: shanshan.shi@polyu.edu.hk (S.S.); yufengzhao@shu.edu.cn (Y.Z.)

Abstract: Due to the environmental friendliness, cost-effectiveness and inherent safety, rechargeable aqueous zinc ion batteries have attracted much interest as a promising energy storage device. VO_2 is one of the most common materials for rechargeable zinc ion batteries. The insertion/extraction of zinc ions within VO_2 is highly anisotropic, with different channel sizes along different axes. Therefore, it is quite important to control the orientation of VO_2 crystals so as to manipulate the transportation of Zn^{2+} ions more effectively and sufficiently. Herein, a novel intercalation-type two-dimensional VO_2 nanosheet with preferred orientation (PO-VO_2) of the c-axis was prepared. Benefitting from the structural merits, the PO-VO_2 nanosheets demonstrate an attractive capacity of 511.6 mAh g^{-1} at a current density of 0.05 A g^{-1} in a voltage of 0.2–1.6 V, which is obviously better than that of many vanadium oxide-based cathodes reported until now. The PO-VO_2//Zn aqueous zinc ion full cell exhibits a high energy density of 290.5 Wh kg^{-1} at a power density of 38.4 W kg^{-1} (based on the mass of the VO_2 cathode electrode). The outstanding energy storage behavior, together with the facile and affordable synthesis route, endows the PO-VO_2 nanosheets with promising applications for aqueous zinc ion batteries.

Keywords: VO_2 nanosheets; preferred orientation; ions transmission channel; aqueous zinc ion batteries

check for updates

Citation: Shi, S.; Yu, Y.; Feng, X.; Qi, R.; Zhao, Y. Two-Dimensional VO_2 Nanosheets with a Controllable Crystalline-Preferred Orientation for High-Performance Zinc-Ion Batteries. *Batteries* **2023**, *9*, 95. https://doi.org/10.3390/batteries9020095

Academic Editor: Carlos Ziebert

Received: 14 December 2022
Revised: 7 January 2023
Accepted: 26 January 2023
Published: 30 January 2023

Copyright: © 2023 by the authors. Licensee MDPI, Basel, Switzerland. This article is an open access article distributed under the terms and conditions of the Creative Commons Attribution (CC BY) license (https://creativecommons.org/licenses/by/4.0/).

1. Introduction

Due to the environmental pollution and excessive carbon emissions caused by traditional fossil fuels consumption, the demand for electrical energy storage (EES) with a high energy density and low cost is increasing, which promotes the development of various renewable and clean energy storage techniques [1–4]. Lithium ion batteries are widely used in our daily life because of their high capacity, high voltage and long cycling performance [5–8]. However, their large-scale application is seriously hindered due to the limited lithium source and high cost. Furthermore, the safety issue of lithium ion batteries based on liquid organic electrolytes remains an unpredictable issue [9,10]. Compared with the other organic batteries systems, the use of aqueous electrolytes is safe and cost-efficient, demonstrating a great potential for practicality [11–15]. As a promising alternative energy storage technology, rechargeable aqueous zinc ion batteries (ZIBs) have attracted tremendous attention because of their high specific capacity (820 mAh g^{-1} and 5855 mAh cm^{-3}), non-toxicity, relatively low redox potential (−0.76 V vs. SHE), inherent safety and cost-effectiveness [16–19].

Preparing suitable cathode materials with a high specific capacity for ZIBs still remains challenging. So far, only a few cathode materials have been explored for ZIBs, such as manganese oxide, vanadium oxide, polyanion and Prussian blue compounds [20–26]. Recently, Wang's group has reported an MnO_2 cathode with a nanocrystal-line structure

by the electrodeposition method for MnO_2//Zn aqueous batteries, which exhibited an outstanding cycling stability, with a capacity decay rate of 0.007% per cycle [20]. NASICON-type $Na_3V_2(PO_4)_3$/C (NVP/C) was first reported by Huang and coworkers as a cathode material for zinc ion batteries. The NVP nanoparticles are wrapped by graphene-like carbon nanosheets, which delivered a high specifical capacity of 97 mAh g^{-1} at 0.5 C between 0.8 and 1.7 V and a discharge voltage plateau at 1.1 V. The mechanism of the insertion/extraction reaction of the $ZnxNaV_2(PO_4)_3$ was also investigated by ex situ X-ray diffraction and X-ray photoelectron spectroscopy [24]. Typically, manganese oxide, as a cathode material for ZIBs, shows a high working voltage and good rate properties. However, due to the Jahn–Teller effect, Mn^{2+} ions are dissolved during the charge–discharge process, so the lifecycle of the manganese oxide electrode is limited [27,28]. Compared to manganese oxide, the stable layered framework in the VO_2 cathode is expected to exhibit an excellent long cycling performance [29]. For example, Zhi and Wu have reported VO_2 hollow spheres that are synthesized by a hydrothermal method as cathode materials for ZIBs. As a result, the as-obtained VO_2 delivers a high specific capacity of 440 mAh g^{-1} at a current density of 0.1 A g^{-1} [30]. Pang's group prepared a composite of VO_2 and amorphous N-doped carbon (VO_2@NC) for zinc ion batteries, and the structure evolution during the charge/discharge processes was also explored by in situ X-ray diffraction measurements [31]. Nevertheless, the VO_2 electrode often shows an unsatisfactory rate performance since it suffers from a large resistance against the diffusion of Zn^{2+} during the insertion/extraction process [32]. Recent studies have made many efforts to deal with these issues. For example, Zhao et al. [23] reported the $MnVO_2$-PVP material by embedding Mn ions as pillars between the layered VO_2 nanostructure, which not only greatly increased the specific capacity and electrochemically active sites but also provided fast ion diffusion kinetics. The synthesized $MnVO_2$-PVP was used as a cathode of zinc ion batteries and realized a high discharge capacity of 176.5 mAh g $^{-1}$ after 5000 cycles at a current density of 10 A g^{-1}. In addition, Liu et al. [33] reported that VO_2 has different sizes of tunnel transport pathways along different axes (0.82 nm^2, 0.34 nm^2 and 0.5 nm^2 along the b-, a- and c-axes, respectively). Herein, controlling the growth of VO_2 with crystalline-preferred orientation plays a crucial role in realizing a high-rate electrochemical performance for ZIBs.

In this work, a two-dimensional VO_2 nanosheet with the preferred growth of the crystal face (as shown in Figure 1) was prepared by a simple hydrothermal method, followed by heat treatment. The schematic representation of the synthesis strategy for PO-VO_2 nanosheets is shown in Figure S1 (Supplementary Materials). The as-prepared PO-VO_2 was used as a cathode material to assemble an aqueous-based zinc ion battery. As shown in Figure 1, the PO-VO_2 nanosheets have preferential orientation growth along the c-axis, which indicates that the as-prepared VO_2 nanosheets can provide more layered ions transport pathways (along the b-axis) than other VO_2 nanosheets without preferential orientation growth. In addition, the VO_2 has the largest size of tunnel transport pathways (0.82 nm^2) along the b-axis (0.34 nm^2 along the a-axis and 0.5 nm^2 along the c-axis, respectively). Therefore, the synthesized PO-VO_2 nanosheets can exhibit an excellent electrochemical performance. As a result, the obtained VO_2 nanosheet exhibits 511.6 mAh g^{-1} at a current density of 0.05 A g^{-1} in a voltage of 0.2–1.6 V. In addition, compared to other vanadium-based zinc ion batteries, the PO-VO_2//Zn aqueous-based zinc ion battery exhibits a higher energy density of 290.5 Wh kg^{-1}. These results show that the VO_2 nanosheet has an excellent electrochemical specific capacity, a high energy density and a power density for aqueous-based ZIBs.

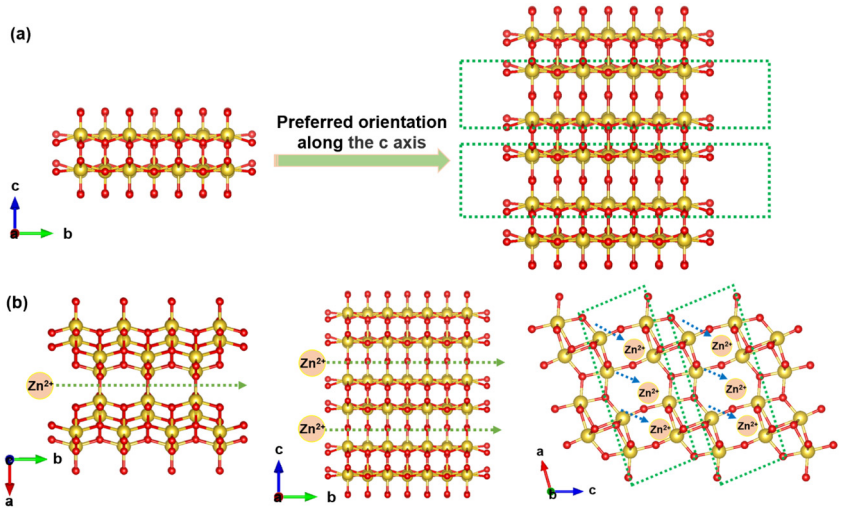


Figure 1. (**a**) Crystal structure of PO-VO_2 nanosheets with preferred orientation along the c-axis. (**b**) Schematic illustration of the zinc ion transmission pathway along the interlamination direction.

2. Experimental Section

Preparation of PO-VO_2: First, 0.3 g of V_2O_5 (AR, 99%) was dissolved in 30 mL of deionized water under magnetic stirring for 1 h. Second, 4 mL of 30% H_2O_2 solution was slowly added into the above solution drop by drop, and the solution turnedbrown. Then, the solution was transferred to the 100 mL stainless steel autoclave and kept at 200 °C for 48 h. When cooled naturally to room temperature, the intermediate products were collected, washed with deionized water/ethanol and dried at 60 °C for 8 h. Third, the intermediate product and thiourea (AR, 99%) were put into two quartz boats with a mass ratio of 1:20. The boat with thiourea was placed at the upstream side of the tube furnace and heated at 350 °C for 6 h in argon atmosphere. Finally, the as-obtained VO_2 material was collected, washed three times with deionized water and dried at 60 °C.

Preparation of the contrast sample VO_2: First, 0.25 g of V_2O_5 powder (AR, 99%) was dissolved in 20 mL of deionized water with 30% H_2O_2 under magnetic stirring for 1 h. Second, 1 g of oxalic acid was added into the above solution and magnetically stirred for 30 min. Then, the solution was transferred to a Teflon hydrothermal reactor and heated at 180 °C for 24 h. The obtained product was centrifuged, washed with water and ethanol several times and dried at 60 °C overnight.

Material Characterization: The X-ray diffraction (XRD) measurement was investigated on D8 X-ray diffraction using Cu Kα radiation from 10 to 85 degrees with a step of 2 degrees/min. The morphology characterization was observed by a field emission scanning electron microscope (FE-SEM, JSM-7500F, 15 kV) and transmission electron microscopy (TEM, JEOL JEM-2100F, 200 kV). X-ray photoelectron spectroscopy (XPS) was characterized by a Thermo escalab 250 Xi spectrometer with an Al Kα X-ray source.

Preparation of PO-VO_2 and VO_2 cathodes: The slurry of PO-VO_2 and VO_2 cathodes was prepared by mixing active material:super P:PVDF, with a mass ratio of 7:2:1, in NMP and stirring for 6 h, followed by casting the slurry onto Ti foil and drying at 120 °C for 10 h in a vacuum oven. The active areas of electrodes were 1.13 cm^2 (φ = 1.2 cm).

Electrochemical characterizations of the full aqueous Zn-ion battery: For the PO-VO_2//Zn full aqueous Zn-ion batteries, the PO-VO_2, as the cathode, the Zn foil, as the anode, and a glass fiber membrane (Whatman, GF/D), as the separator, were assembled in CR2032 coin cells under air conditions. The electrolyte was 3M $Zn(CF_3SO_3)_2$, with deionized water as the solvent. The number of electrolytes (150 μL) for each cell is the same. The assembly process of the VO_2//Zn aqueous Zn-ion batteries is the same as that of the PO-VO_2//Zn batteries. The galvanostatic charge–discharge tests of PO-VO_2//Zn and VO_2//Zn batteries were performed by using LAND CT2001 at room temperature in the potential range of 0.2–1.4 V, 0.2–1.5 V and 0.2–1.6 V, respectively. The cyclic voltammetry

(CV) curves were evaluated on CHI760E (Chenhua electrochemical station) at a scan rate of 0.1 mV s^{-1} and a voltage of 0.2–1.5 V. The electrochemical impedance spectroscopy (EIS) measurements of the PO-VO_2//Zn and VO_2//Zn batteries were collected in a 2032 coin cell by using AC amplitude with a frequency range of 0.01 Hz~100 kHz via the CHI760E electrochemical workstation.

3. Results and Discussion

The PO-VO_2 nanosheet was synthesized by the hydrothermal method, followed by a reduction reaction, using thiourea as the reductant. The detailed preparation processes of the PO-VO_2 nanosheet and the contrast VO_2 nanosheet without preferred orientation growth are shown in the Experimental Section and Figure S1 (Supplementary Materials). The crystal structure of the PO-VO_2 nanosheet was investigated by X-ray diffraction (XRD). All characteristic peaks in Figure 2a are in agreement with the standard card of VO_2 (JCPDS No. 31-1438) [34]. Especially, in Figure 2a, the strongest diffraction peak at 29° corresponds to the (002) plane, and the relative intensity ratio of (002)/(110) is higher than the standard values in the JCPDS card, indicating that the as-prepared VO_2 nanosheets had preferential orientation growth along the (002) plane [35–37]. Similar phenomena were found in the (001) and (003) planes, which demonstrates that PO-VO_2 nanosheets have preferential orientation growth along the c-axis. The XRD patterns of the contrast VO_2 nanosheet are shown in Figure S2 (Supplementary Materials). All peaks can be indexed to the pure VO_2 phase without any impurity peaks. From the XRD patterns of the PO-VO_2 and contrast VO_2 materials, we can find that the PO-VO_2 nanosheets have the preferred growth orientation, while the contrast VO_2 does not have this character. The X-ray photoelectron spectroscopy (XPS) was used to explore the composition and elemental valence states of the as-prepared PO-VO_2. The binding energies of all observed peaks were corrected with the C1s (284.5 eV) reference peak. The XPS survey spectrum (Figure 2b) displays obvious characteristic peaks of V and O. The two distinct peaks in the O 1s XPS spectrum (Figure 2c) at binding energies of 530.2 eV and 531.1 eV are attributed to the V-O of the PO-VO_2 and C-O bonds, respectively. The V $2p_{3/2}$ spectrum (Figure 2d) can be deconvoluted into two peaks at binding energies of 515.9 eV and 517.0 eV, which could be ascribed to V^{4+} and V^{5+}, respectively [34,38]. The V^{5+} species originate from the oxidized VO_2 in contact with the air, which is commonly found in the vanadium oxide materials. The peak located at 523.4 eV and 524.3 eV can be indexed to the V $2p_{1/2}$ spectrum. These XPS analyses demonstrate the successful synthesis of VO_2, which is consistent with the XRD results.

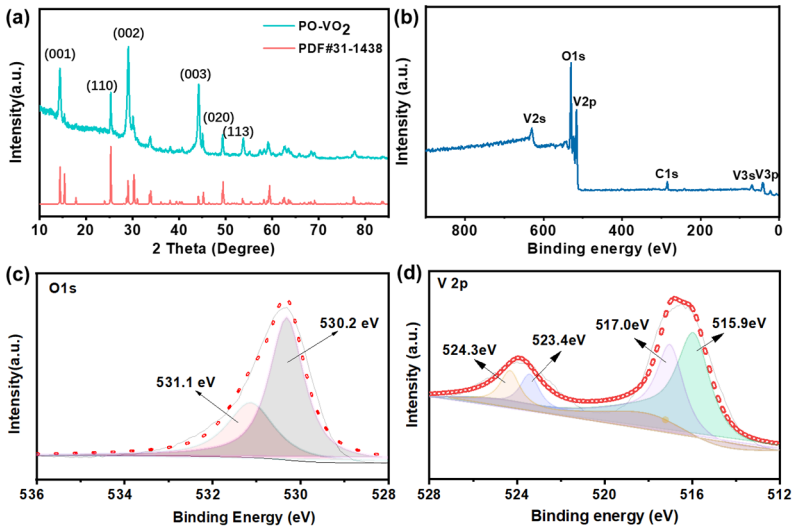


Figure 2. (**a**) The XRD pattern of the PO-VO_2 nanosheet; (**b**) the XPS survey spectrum; (**c**) the O 1s and (**d**) V 2p spectrum of the PO-VO_2 nanosheet.

The morphology and microstructures of the PO-VO_2 nanosheet were characterized by field emission scanning electron microscopy (FE-SEM) and transmission electron microscopy (TEM). Figure 3a,b and Figure S3 (Supplementary Materials) show that the PO-VO_2 material is composed of uniform nanosheets. Furthermore, the TEM images in Figure 3c,d demonstrate that the ultrathin VO_2 nanosheets have a smooth surface. The interplanar spacing in the high-resolution transmission electron microscopy (HR-TEM image, Figure 3e) is 3.1 Å, corresponding to the (002) planes, which is consistent with the XRD results. Furthermore, the selected area electron diffraction (SAED) pattern (Figure 3f) demonstrates distinct diffraction spots which correspond to the (002) plane of monoclinic VO_2 nanosheets. In addition, the energy-dispersive X-ray spectra (EDS) mappings of the as-obtained PO-VO_2 display that V and O elements are distributed homogeneously in the sample (Figure 3g–i). The above results indicate that the as-prepared nanosheet was a VO_2 phase with high purity. The unique layered nanosheet structure can provide efficient pathways for the diffusion of zinc ions, enabling a high specific capacity and fast charge–discharge performance.

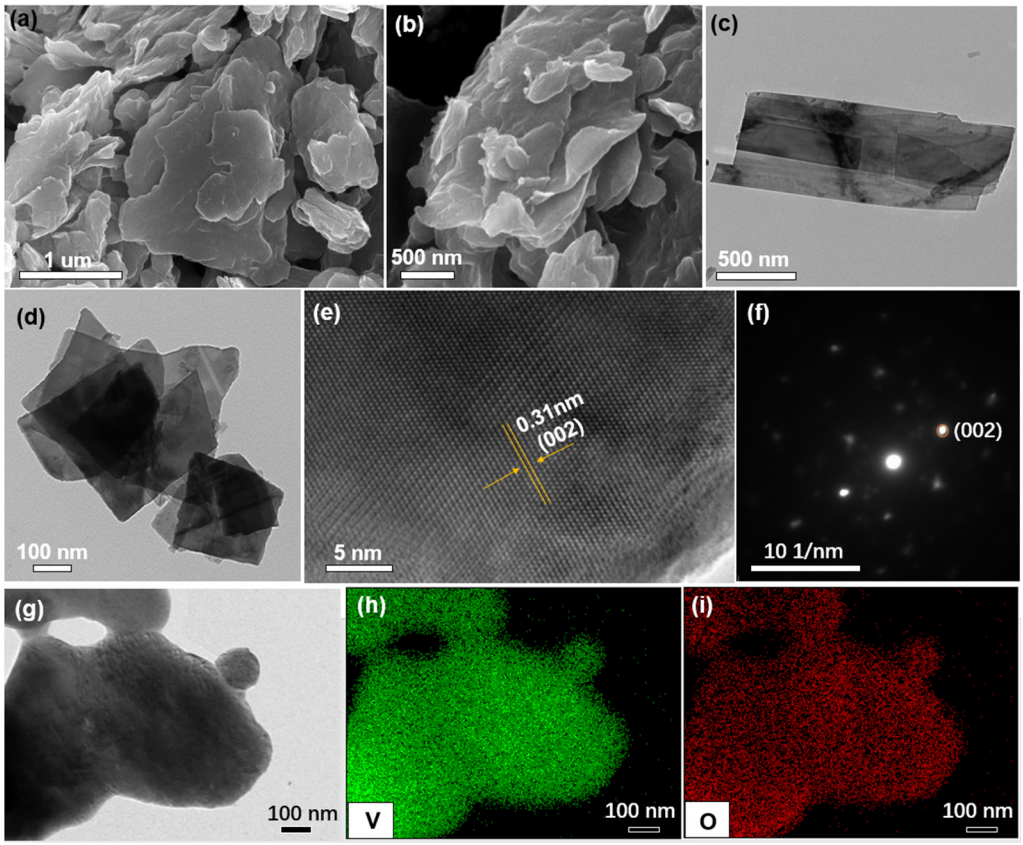


Figure 3. The morphology of VO_2 2D-nanosheets: (**a**,**b**) SEM images; (**c**,**d**) TEM images; (**e**) HR-TEM image; (**f**) SAED pattern; (**g**–**i**) TEM image and corresponding element mappings of V and O.

In order to explore the potential application of PO-VO_2 material, the as-prepared PO-VO_2 nanosheets' cathode and Zn foil anode were assembled in a coin-type cell with 3 M [$Zn(CF_3SO_3)_2$] as the electrode. The electrochemical performances of the PO-VO_2//Zn aqueous ZIBs were measured by the LAND battery test system at different voltages of 0.2–1.4 V, 0.2–1.5 V and 0.2–1.6 V, respectively. Figure 4 shows the rate performance at different current densities and the corresponding galvanostatic charge–discharge curves at 0.05 A g^{-1} in the different voltage ranges. From Figure 4a, we can find that the reversible discharge capacities are 264.4, 255.8, 245.7, 227.8, 211.8, 177.6, 130.5 and 80.4 mAh g^{-1} at a current density of 0.05, 0.1, 0.2, 0.3, 0.5, 1.0, 2.0 and 3.0 A g^{-1} under a voltage of 0.2–1.4 V (vs. Zn/Zn^{2+}), respectively. Furthermore, the discharge specific capacity retains

257.5 mAh g^{-1} when the current density is back to 0.05 A g^{-1}, with a capacity retention of 97.4%, demonstrating an excellent rate performance. The galvanostatic charge–discharge curves in Figure 4b exhibit a voltage slop region around 0.3–0.7 V, and this indicates that the redox reaction takes place during the Zn^{2+} ions intercalation/deintercalation process. Figure 4c shows the rate performance in the voltage range of 0.2–1.5 V. When the current density is 0.05, 0.1, 0.2, 0.3, 0.5, 1.0 and 2.0 A g^{-1}, the specific discharge capacity is 393.6, 371.6, 341.9, 290.1, 226.9, 184.9 and 119.8 mAh g^{-1}, respectively. When the current density returns to 0.05 A g^{-1}, the specific discharge capacity recovers to 329 mAh g^{-1}, which has reached 83.6% of the initial capacity, showing a good rate performance. The gradually increased reversible capacity during the first several cycles may be ascribed to the consistent activation of the PO-VO_2 nanosheets cathode during the cycling, where the electrolyte gradually infiltrates into the electrode material, which is commonly observed in the metal oxide materials [23].

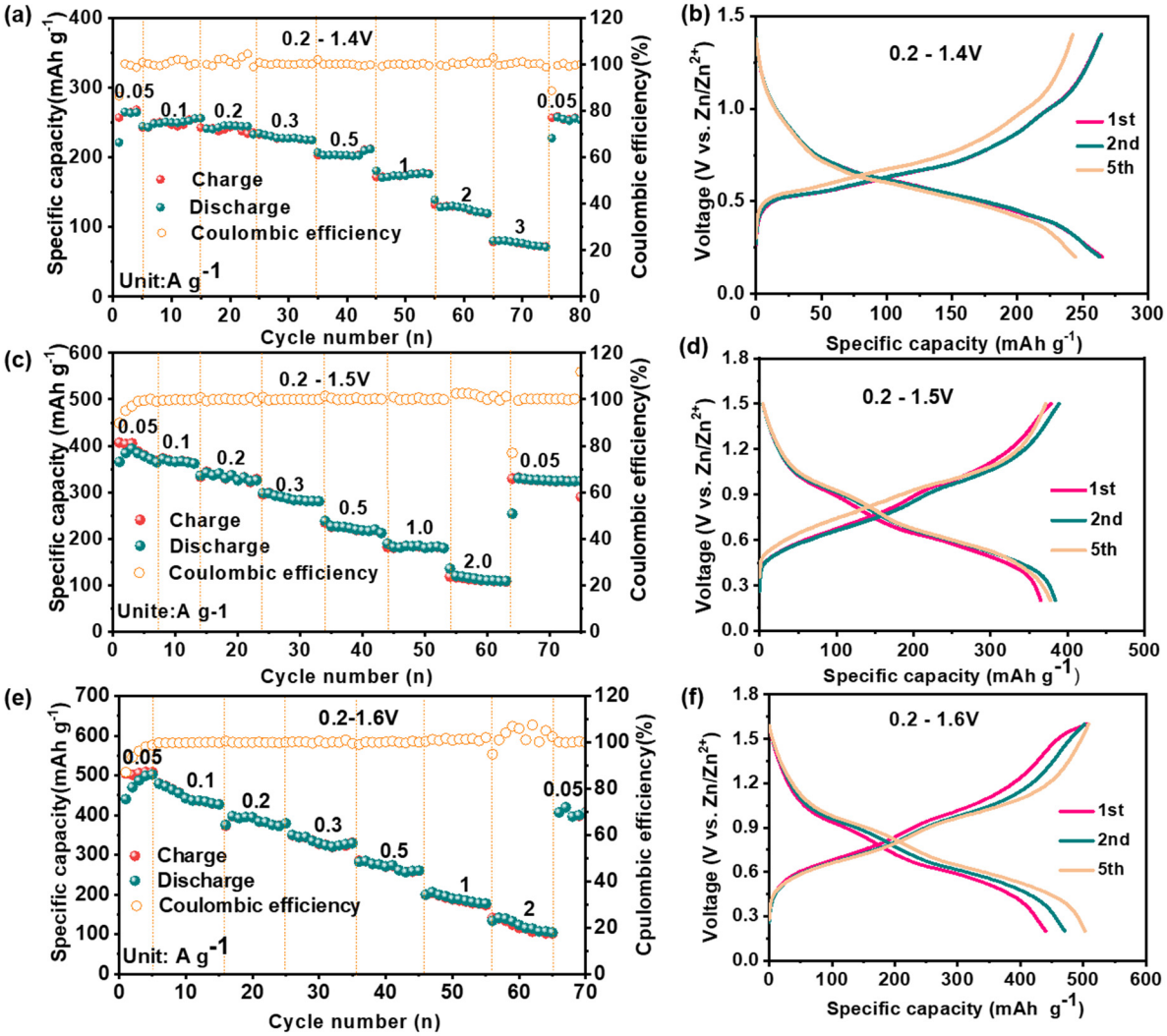


Figure 4. The electrochemical performance of PO-VO_2//Zn batteries: (**a**,**b**) the rate performance at different current densities and corresponding galvanostatic charge-discharge curves in the voltage of 0.2–1.4 V; (**c**,**d**) the rate performance at different current densities and corresponding galvanostatic charge-discharge curves in the voltage of 0.2–1.5 V; (**e**,**f**) the rate performance at different current densities and corresponding galvanostatic charge-discharge curves in the voltage of 0.2–1.6 V.

To investigate the effects of the voltage window on the electrochemical performance, the performance of PO-VO_2 nanosheets in the potential range of 0.2–1.6 V is shown in Figure 4e. When the current density is 0.05, 0.1, 0.2, 0.3, 0.5, 1.0 and 2.0 A g^{-1}, the

corresponding specific discharge capacity is 511.6, 432.8, 393.7, 310.2, 263.8, 182.6 and 102.5 mAh g^{-1}, respectively. When the current density returns to 0.05 A g^{-1}, the specific discharge capacity recovers to 403.5 mAh g^{-1} and reaches 78.9% of the initial capacity. Although the initial capacity of the material is high in this voltage range, the rate performance is poor. These results indicate that different voltage ranges have a large influence on the rate capability of PO-VO_2 nanosheets. Specifically, the capacity will increase as the potential window improves gradually, but the rate performance at a high current density will become worse. The voltage window of a battery refers to the voltage range involving the reversible chemical reactions of the electrode during the charge and discharge process. The voltage window of the battery refers to the voltage range in which involving reversible chemical reaction of the electrodes during charging and discharging. In principle, the charging and discharging process of the energy storage device requires an oxidation reaction on the cathode and a reduction on the anode electrode. A number of aqueous energy storage devices have explored a maximum charging voltage higher than the thermodynamic breakdown window of water [13]. The maximum charging voltage corresponds to the fully charged state of a battery, which is usually dependent on the irreversible redox reactions on the electrodes or electrolyte decomposition. Under the maximum voltage, there is a region where the device can store energy by ions intercalation/deintercalation processes between the cathode and anode. Therefore, the capacities are strongly affected by the voltage window. As a comparison, the rate performance of the contrast VO_2 nanosheets without preferential orientation growth is shown in Figure S4 (Supplementary Materials). These results manifest that the as-prepared PO-VO_2 nanosheets can exhibit an excellent electrochemical performance because the PO-VO_2 can provide more layered ions transport pathways than other VO_2 nanosheets without preferential orientation growth. In addition, the VO_2 has the largest size of tunnel transport pathways along the b-axis (0.82 nm^2).

The cyclic voltammetry of PO-VO_2//Zn batteries (Figure 5a) was carried out at a voltage of 0.2–1.5 V, with a scan rate of 0.1 mV s^{-1}. The separated anode peaks at 0.59 V and 0.93 V and the cathode peaks at 0.48 V and 1.02 V correspond to multistep intercalation/deintercalation processes. In the following charge/discharge process, all the cathode and anode peaks are similar to those of the first cycle, indicating the good reversibility of VO_2 nanosheets. The cycling stability of the PO-VO_2//Zn battery was conducted at a current density of 1 A g^{-1} under the different voltage ranges of 0.2–1.4 V, 0.2–1.5 V and 0.2–1.6 V, respectively. As shown in Figure 5b, when the voltage range is 0.2–1.4 V, the discharge specific capacity of the material first increases and then decreases, with discharge specific capacities of 128.6 mAh g^{-1} and 136.0 mAh g^{-1} at the first and 400th cycles, respectively, showing a capacity retention rate of 105.8%. In the voltage range of 0.2–1.5 V, the Zn//VO_2 battery exhibits 210.1 mAh g^{-1} and 205.5 mAh g^{-1} in the first and 400th cycles, respectively (Figures 5b and S5), with a capacity retention rate of 97.8%. Meanwhile, as a comparison, the contrast sample VO_2 without preferred orientation delivered a much lower specific capacity than PO-VO_2 (Figures S6 and S7, Supplementary Materials); it is manifested that the crystalline-preferred orientation along the c-axis by the structural engineering method can greatly improve the electrochemical performance of VO_2 nanosheets. When the voltage range is 0.2–1.6 V, the initial capacity of the PO-VO_2//Zn battery is 180.9 mAh g^{-1}. After 200 cycles, the specific discharge capacity is only 79.1 mAh g^{-1}, and the capacity retention rate is only 43.7%. By contrast, these results indicate that the performance of the battery is poor when it is cycled under the voltage range of 0.2–1.6 V, and the material shows an excellent retention capacity in the ranges of 0.2–1.4 V and 0.2–1.5 V. However, the capacity of the PO-VO_2 nanosheets is better in the voltage range of 0.2–1.5 V. A probable reason for this is that the electrolyte will be oxidized at a high charging voltage and will generate some by-products, which will block the electrode micropores and hinder the transmission of Zn^{2+} ions, thus causing capacity fading during the cycling [39].

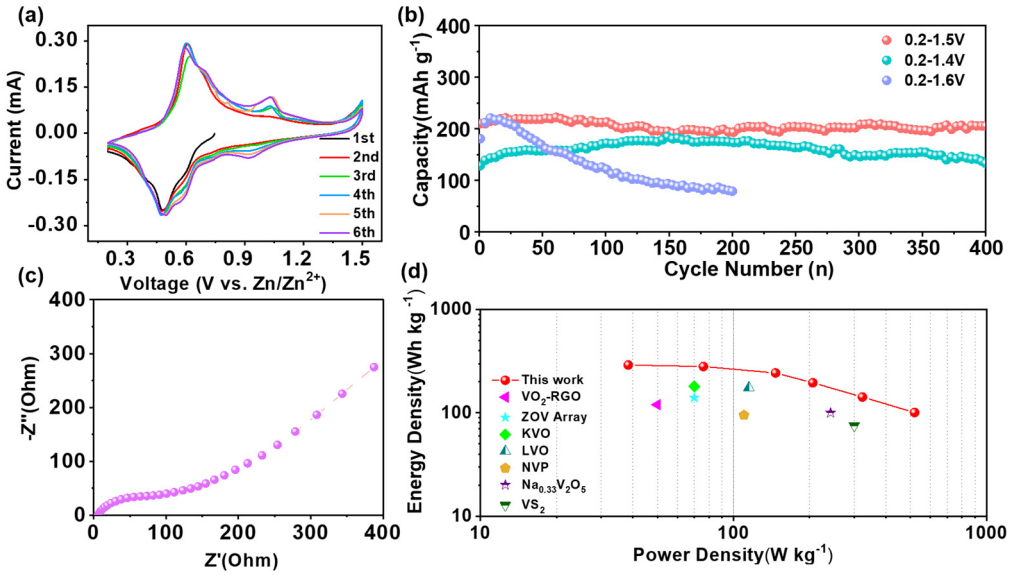


Figure 5. (**a**) The first several cycle CV curves of PO-VO_2//Zn batteries at a voltage of 0.2–1.5 V; (**b**) the cycling performance at a current density of 1 A g^{-1} under the different voltage range; (**c**) the EIS plot at 0.01–10^6 Hz; (**d**) comparison of the energy density and power density of the VO_2//Zn battery with reported ZIBs based on different electrodes.

In order to further study the electrochemical dynamic performance of the PO-VO_2//Zn battery, electrochemical impedance spectroscopy (EIS) was carried out in the frequency range of 0.01 Hz to 10^6 Hz. The results are shown in Figure 5c and Figure S8 (Supplementary Materials). The Nyquist curve consists of a semicircle in the high-frequency region and an oblique straight line in the low-frequency region. The value of the first intersection point between the semicircle and the x-axis in the high-frequency region is the internal resistance of the electrode, while the semicircle is related to the electrolyte resistance and charge transfer resistance (Rct) [40]. The oblique line in the low-frequency region represents the diffusion process of ions in the battery, which is related to the electrochemical performance of the sample. It can be seen in Figure 5c that the charge transfer internal resistance of VO_2 nanosheets is much smaller than that of the contrast VO_2 (Figure S8, Supplementary Materials), which indicates the rapid ion transport in the aqueous zinc ion battery. Figure 5d shows the Ragone plot of the aqueous-based VO_2//Zn battery. The PO-VO_2//Zn battery can achieve an energy density of 290.5 Wh kg^{-1} at a power density of 38.4 W kg^{-1} (based on the mass of the VO_2 cathode electrode). Compared with those reported works (VO_2-rGO//Zn [32], layered zinc orthovanadate ZOV Array//Zn [41], $K_2V_6O_{16}{\cdot}2.7H_2O$//Zn [42], lithium vanadium oxide LVO//Zn [43], $Na_3V_2(PO_4)_3$//Zn [24], $Na_{0.33}V_2O_5$//Zn [44], VS_2//Zn [45]), the aqueous-based PO-VO_2//Zn cell shows a much higher energy density and power density, which indicates that the PO-VO_2 nanosheets prepared in this experiment are among the most promising cathode materials for aqueous-based zinc ion batteries.

4. Conclusions

In this work, the PO-VO_2 nanosheets with a smooth surface and crystalline-preferred orientation along the c-axis were prepared by the simple hydrothermal method, followed by low-temperature heat treatment using V_2O_5 as a raw material and thiourea as a reducing agent. The as-obtained PO-VO_2 nanosheet was assembled as the cathode material for a PO-VO_2//Zn aqueous-based zinc ion full battery. Benefitting from the structural merits, the PO-VO_2 nanosheets provide more ions transportation pathways along the b-axis for the insertion/extraction of zinc ions, which exhibits an attractive capacity of 511.6 mAh g^{-1} at a current density of 0.05 A g^{-1} in a voltage of 0.2–1.6 V. Those excellent electrochemical performances are obviously better than those of many vanadium oxide-based cathodes reported until now. In addition, the PO-VO_2//Zn aqueous zinc ion full cell exhibits a high

energy density of 290.5 Wh kg^{-1} at a power density of 38.4 W kg^{-1} (based on the mass of the VO_2 cathode electrode). The outstanding energy storage behavior, together with the facile and affordable synthesis route, endows the PO-VO_2 nanosheets with promising applications for aqueous zinc ion batteries.

Supplementary Materials: The following supporting information can be downloaded at: https://www.mdpi.com/article/10.3390/batteries9020095/s1, Figure S1: Schematic representation of the synthesis strategy for PO-VO_2 nanosheets; Figure S2: XRD patterns of the contrast sample VO_2; Figure S3: (a,b) SEM images of PO-VO_2 nanosheets; Figure S4: The rate performance of the contrast sample VO_2 at different current densities at a voltage of 0.2–1.5 V; Figure S5: The galvanostatic charge–discharge curves of PO-VO_2 in different cycle numbers at a voltage of 0.2–1.5 V and a current density of 1 A g^{-1}; Figure S6: The galvanostatic charge–discharge curves of the contrast sample VO_2 in different cycle numbers at a voltage of 0.2–1.5 V at a current density of 0.1 A g^{-1}; Figure S7: The cycling performance of the contrast sample VO_2 at a current density of 0.1 A g^{-1} at a voltage of 0.2–1.5 V; Figure S8: The EIS plot of the contrast VO_2 at 0.01–10^6 Hz.

Author Contributions: Conceptualization, S.S. and Y.Z.; methodology, Y.Y.; software, X.F.; formal analysis, R.Q.; investigation, S.S. and Y.Y.; resources, S.S.; data curation, S.S. and Y.Y.; writing—original draft preparation, S.S.; writing—review and editing, Y.Z.; supervision, Y.Z.; project administration, Y.Z.; funding acquisition, Y.Z. and S.S. All authors have read and agreed to the published version of the manuscript.

Funding: This research was funded by the opening fund of National Engineering Research Center of Phosphorus Resources Development and Utilization (NECP2022-06), the National Natural Science Foundation of China (51774251), the Hebei Natural Science Foundation for Distinguished Young Scholars (B2017203313), the Hundred Excellent Innovative Talents Support Program in Hebei Province (SLRC2017057), the Talent Engineering Training Funds of Hebei Province (A201802001).

Data Availability Statement: The data presented in this study are available on request from the corresponding author.

Conflicts of Interest: The authors declare no conflict of interest.

References

1. Li, Y.; Shi, Q.; Yin, X.; Wang, J.; Wang, J.; Zhao, Y.; Zhang, J. Construction Nasicon-Type $NaTi_2(PO_4)_3$ Nanoshell on the surface of P2-type $Na_{0.67}Co_{0.2}Mn_{0.8}O_2$ Cathode as Superior Room/Low-Temperature Sodium Storage. *Chem. Eng. J.* **2020**, *402*, 126181. [CrossRef]
2. Xu, X.; Liu, J.; Liu, J.; Ouyang, L.; Hu, R.; Wang, H.; Yang, L.; Zhu, M. A General Metal-Organic Framework (MOF)-Derived Selenidation Strategy for In Situ Carbon-Encapsulated Metal Selenides as High-Rate Anodes for Na-Ion Batteries. *Adv. Funct. Mater.* **2018**, *28*, 1707573. [CrossRef]
3. Shi, S.; Sun, C.; Yin, X.; Shen, L.; Shi, Q.; Zhao, K.; Zhao, Y.; Zhang, J. FeP Quantum Dots Confined in Carbon-Nanotube-Grafted P-Doped Carbon Octahedra for High-Rate Sodium Storage and Full-Cell Applications. *Adv. Funct. Mater.* **2020**, *30*, 1909283. [CrossRef]
4. Liu, S.; Kang, L.; Jun, S.C. Challenges and Strategies toward Cathode Materials for Rechargeable Potassium-Ion Batteries. *Adv. Mater.* **2021**, *33*, 2004689. [CrossRef] [PubMed]
5. Tarascon, J.M.; Armand, M. Issues and challenges facing rechargeable lithium batteries. *Nature* **2001**, *414*, 359–367. [CrossRef] [PubMed]
6. Goodenough, J.B.; Park, K.-S. The Li-Ion Rechargeable Battery: A Perspective. *J. Am. Chem. Soc.* **2013**, *135*, 1167–1176. [CrossRef] [PubMed]
7. Schmuch, R.; Wagner, R.; Hörpel, G.; Placke, T.; Winter, M. Performance and cost of materials for lithium-based rechargeable automotive batteries. *Nat. Energy* **2018**, *3*, 267–278. [CrossRef]
8. Kang, L.; Zhang, M.; Zhang, J.; Liu, S.; Zhang, N.; Yao, W.J.; Ye, Y.; Luo, C.; Gong, Z.W.; Wang, C.L.; et al. Dual-defect surface engineering of bimetallic sulfide nanotubes towards flexible asymmetric solid-state supercapacitors. *J. Mater. Chem. A* **2020**, *8*, 24053–24064. [CrossRef]
9. Shi, S.; Li, Z.; Shen, L.; Yin, X.; Liu, Y.; Chang, G.; Wang, J.; Xu, S.; Zhang, J.; Zhao, Y. Electrospun free-standing FeP@NPC film for flexible sodium ion batteries with remarkable cycling stability. *Energy Storage Mater.* **2020**, *29*, 78–83. [CrossRef]
10. Yin, X.; Sarkar, S.; Shi, S.; Huang, Q.-A.; Zhao, H.; Yan, L.; Zhao, Y.; Zhang, J. Recent Progress in Advanced Organic Electrode Materials for Sodium-Ion Batteries: Synthesis, Mechanisms, Challenges and Perspectives. *Adv. Funct. Mater.* **2020**, *30*, 1908445. [CrossRef]

11. Kim, H.; Hong, J.; Park, K.-Y.; Kim, H.; Kim, S.-W.; Kang, K. Aqueous Rechargeable Li and Na Ion Batteries. *Chem. Rev.* **2014**, *114*, 11788–11827. [CrossRef]
12. Liang, Y.; Jing, Y.; Gheytani, S.; Lee, K.-Y.; Liu, P.; Facchetti, A.; Yao, Y. Universal quinone electrodes for long cycle life aqueous rechargeable batteries. *Nat. Mater.* **2017**, *16*, 841–848. [CrossRef]
13. Dai, Z.; Peng, C.; Chae, J.H.; Ng, K.C.; Chen, G.Z. Cell voltage versus electrode potential range in aqueous supercapacitors. *Sci. Rep.* **2015**, *5*, 9854. [CrossRef]
14. Su, D.; McDonagh, A.; Qiao, S.-Z.; Wang, G. High-Capacity Aqueous Potassium-Ion Batteries for Large-Scale Energy Storage. *Adv. Mater.* **2017**, *29*, 1604007. [CrossRef] [PubMed]
15. Parker, J.F.; Chervin, C.N.; Pala, I.R.; Machler, M.; Burz, M.F.; Long, J.W.; Rolison, D.R. Rechargeable nickel-3D zinc batteries: An energy-dense, safer alternative to lithium-ion. *Science* **2017**, *356*, 414–417. [CrossRef]
16. Wang, X.; Wang, F.; Wang, L.; Li, M.; Wang, Y.; Chen, B.; Zhu, Y.; Fu, L.; Zha, L.; Zhang, L.; et al. An Aqueous Rechargeable Zn//Co_3O_4 Battery with High Energy Density and Good Cycling Behavior. *Adv. Mater.* **2016**, *28*, 4904–4911. [CrossRef] [PubMed]
17. Zeng, Y.; Meng, Y.; Lai, Z.; Zhang, X.; Yu, M.; Fang, P.; Wu, M.; Tong, Y.; Lu, X. An Ultrastable and High-Performance Flexible Fiber-Shaped Ni-Zn Battery based on a Ni-NiO Heterostructured Nanosheet Cathode. *Adv. Mater.* **2017**, *29*, 1702698. [CrossRef] [PubMed]
18. Xia, C.; Guo, J.; Li, P.; Zhang, X.; Alshareef, H.N. Highly Stable Aqueous Zinc-Ion Storage Using a Layered Calcium Vanadium Oxide Bronze Cathode. *Angew. Chem. Int. Ed.* **2018**, *57*, 3943–3948. [CrossRef]
19. Soundharrajan, V.; Sambandam, B.; Kim, S.; Alfaruqi, M.H.; Putro, D.Y.; Jo, J.; Kim, S.; Mathew, V.; Sun, Y.-K.; Kim, J. $Na_2V_6O_{16}$ center dot 3H(2)O Barnesite Nanorod: An Open Door to Display a Stable and High Energy for Aqueous Rechargeable Zn-Ion Batteries as Cathodes. *Nano Lett.* **2018**, *18*, 2402–2410. [CrossRef] [PubMed]
20. Sun, W.; Wang, F.; Hou, S.; Yang, C.; Fan, X.; Ma, Z.; Gao, T.; Han, F.; Hu, R.; Zhu, M.; et al. Zn/MnO_2 Battery Chemistry With H^+ and Zn^{2+} Coinsertion. *J. Am. Chem. Soc.* **2017**, *139*, 9775–9778. [CrossRef] [PubMed]
21. He, D.; Sun, T.; Wang, Q.; Ma, T.; Zheng, S.; Tao, Z.; Liang, J. Multi-Functional Potassium Ion Assists Ammonium Vanadium Oxide Cathode for High-Performance Aqueous Zinc-Ion Batteries. *Batteries* **2022**, *8*, 84. [CrossRef]
22. Senguttuvan, P.; Han, S.-D.; Kim, S.; Lipson, A.L.; Tepavcevic, S.; Fister, T.T.; Bloom, I.D.; Burrell, A.K.; Johnson, C.S. A High Power Rechargeable Nonaqueous Multivalent Zn/V_2O_5 Battery. *Adv. Energy Mater.* **2016**, *6*, 1600826. [CrossRef]
23. Liu, Y.; Zou, Y.N.; Guo, M.Y.; Hui, Z.X.; Zhao, L.J. Boosting the active sites and kinetics of VO_2 by Mn pre-intercalated and PVP modified nanostructure to improve the cycle stability for aqueous zinc batteries. *Chem. Eng. J.* **2022**, *433*, 133528. [CrossRef]
24. Li, G.; Yang, Z.; Jiang, Y.; Jin, C.; Huang, W.; Ding, X.; Huang, Y. Towards polyvalent ion batteries: A zinc-ion battery based on NASICON structured. *Nano Energy* **2016**, *25*, 211–217. [CrossRef]
25. Zhao, Q.; Huang, W.; Luo, Z.; Liu, L.; Lu, Y.; Li, Y.; Li, L.; Hu, J.; Ma, H.; Chen, J. High-capacity aqueous zinc batteries using sustainable quinone electrodes $Na_3V_2(PO_4)_3$. *Sci. Adv.* **2018**, *4*, 1761. [CrossRef]
26. Du, Y.H.; Liu, X.Y.; Wang, X.Y.; Sun, J.C.; Lu, Q.Q.; Wang, J.Z.; Omar, A.; Mikhailova, D. Freestanding strontium vanadate/carbon nanotube films for long-life aqueous zinc-ion batteries. *Rare Met.* **2022**, *41*, 415–424. [CrossRef]
27. Wang, J.; Wang, J.-G.; Liu, H.; Wei, C.; Kang, F. Zinc ion stabilized MnO_2 nanospheres for high capacity and long lifespan aqueous zinc-ion batteries. *J. Mater. Chem. A* **2019**, *7*, 13727–13735. [CrossRef]
28. Song, M.; Tan, H.; Chao, D.; Fan, H.J. Recent Advances in Zn-Ion Batteries. *Adv. Funct. Mater.* **2018**, *28*, 1802564. [CrossRef]
29. Ding, J.; Du, Z.; Gu, L.; Li, B.; Wang, L.; Wang, S.; Gong, Y.; Yang, S. Ultrafast Zn^{2+} Intercalation and Deintercalation in Vanadium Dioxide. *Adv. Mater.* **2018**, *30*, 1800762. [CrossRef]
30. Liu, Y.; Hu, P.F.; Liu, H.Q.; Wu, X.; Zhi, C.Y. Tetragonal VO_2 hollow nanospheres as robust cathode materials for aqueous zinc ion batteries. *Mater. Today Energy* **2020**, *17*, 100431. [CrossRef]
31. Lv, T.T.; Luo, X.; Yuan, G.Q.; Yang, S.Y.; Pang, H. Layered VO_2@ N-doped carbon composites for high-performance rechargeable aqueous zinc-ion batteries. *Chem. Eng. J.* **2022**, *428*, 131211. [CrossRef]
32. Dai, X.; Wan, F.; Zhang, L.; Cao, H.; Niu, Z. Freestanding graphene/VO_2 composite films for highly stable aqueous Zn-ion batteries with superior rate performance. *Energy Storage Mater.* **2019**, *17*, 143–150. [CrossRef]
33. Liu, Q.; Tan, G.; Wang, P.; Abeyweera, S.C.; Zhang, D.; Rong, Y.; Wu, Y.A.; Lu, J.; Sun, C.-J.; Ren, Y.; et al. Revealing mechanism responsible for structural reversibility of single-crystal VO_2 nanorods upon lithiation/delithiation. *Nano Energy* **2017**, *36*, 197–205. [CrossRef]
34. Wang, J.; Zhang, X.; Zhang, Y.; Abas, A.; Zhao, X.; Yang, Z.; Su, Q.; Lan, W.; Xie, E. Lightweight, interconnected VO_2 nanoflowers hydrothermally grown on 3D graphene networks for wide-voltage-window supercapacitors. *RSC Adv.* **2017**, *7*, 35558–35564. [CrossRef]
35. Liu, Z.; Wen, X.D.; Wu, X.L.; Gao, Y.J.; Chen, H.T.; Zhu, J.; Chu, P.K. Intrinsic Dipole-Field-Driven Mesoscale Crystallization of Core-Shell ZnO Mesocrystal Microspheres. *J. Am. Chem. Soc.* **2009**, *131*, 9405–9412. [CrossRef] [PubMed]
36. Kim, H.; Camata, R.; Chowdhury, S.; Vohrab, Y. In vitro dissolution and mechanical behavior of c-axis preferentially oriented hydroxyapatite thin films fabricated by pulsed laser deposition. *Acta Biomater.* **2010**, *6*, 3234–3241. [CrossRef]
37. Song, G.Y.; Oh, C.; Sinha, S.; Son, J.; Heo, J. Facile phase control of multivalent vanadium oxide thin films (V_2O_5 and VO_2) by atomic layer deposition and postdeposition annealing. *ACS Appl. Mater. Interfaces* **2017**, *9*, 23909–23917. [CrossRef]
38. Silversmit, G.; Depla, D.; Poelman, H.; Marin, G.B.; De Gryse, R. Determination of the V2p XPS binding energies for different vanadium oxidation states (V^{5+} to V^{0+}). *J. Electron Spectrosc. Relat. Phenom.* **2004**, *135*, 167–175. [CrossRef]

39. Luo, H.; Wang, B.; Wang, F.; Yang, J.; Wu, F.D.; Ning, Y.; Zhou, Y.; Wang, D.L.; Liu, H.K.; Dou, S.X. Anodic oxidation strategy toward structure-optimized V_2O_3 cathode via electrolyte regulation for Zn-ion storage. *ACS Nano* **2020**, *14*, 7328–7337. [CrossRef]
40. Rudy, A.; Mironenko, A.; Naumov, V.; Novozhilova, A.; Skundin, A.; Fedorov, I. Determination of Diffusion Coefficients of Lithium in Solid Electrolyte LiPON. *Batteries* **2021**, *7*, 21. [CrossRef]
41. Chao, D.; Zhu, C.; Song, M.; Liang, P.; Zhang, X.; Tiep, N.; Zhao, H.; Wang, J.; Wang, R.; Zhang, H.; et al. A High-Rate and Stable Quasi-Solid-State Zinc-Ion Battery with Novel 2D Layered Zinc Orthovanadate Array. *Adv. Mater.* **2018**, *30*, 1803181. [CrossRef]
42. Sambandam, B.; Soundharrajan, V.; Kim, S.; Alfaruqi, M.; Jo, J.; Kim, S.; Mathew, V.; Sun, Y.; Kim, J. $K_2V_6O_{16}{\cdot}2.7H_2O$ nanorod cathode: An advanced intercalation system for high energy aqueous rechargeable Zn-ion batteries. *J. Mater. Chem. A* **2018**, *6*, 15530–15539. [CrossRef]
43. Alfaruqi, M.; Mathew, V.; Song, J.; Kim, S.; Islam, S.; Pham, D.; Jo, J.; Kim, S.; Baboo, J.; Xiu, Z.; et al. Electrochemical zinc intercalation in lithium vanadium oxide: A high-capacity zinc-ion battery cathode. *Chem. Mater.* **2017**, *29*, 1684–1694. [CrossRef]
44. He, P.; Zhang, G.; Liao, X.; Yan, M.; Xu, X.; An, Q.; Liu, J.; Mai, L. Sodium Ion Stabilized Vanadium Oxide Nanowire Cathode for High-Performance Zinc-Ion Batteries. *Adv. Energy Mater.* **2018**, *8*, 1702463. [CrossRef]
45. He, P.; Yan, M.; Zhang, G.; Sun, R.; Chen, L.; An, Q.; Mai, L. Layered VS_2 Nanosheet-Based Aqueous Zn Ion Battery Cathode. *Adv. Energy Mater.* **2017**, *7*, 160192. [CrossRef]

Disclaimer/Publisher's Note: The statements, opinions and data contained in all publications are solely those of the individual author(s) and contributor(s) and not of MDPI and/or the editor(s). MDPI and/or the editor(s) disclaim responsibility for any injury to people or property resulting from any ideas, methods, instructions or products referred to in the content.